

## Structures of the stator complex that drives rotation of the bacterial flagellum

Justin C. Deme<sup>1,2</sup>, Steven Johnson<sup>1</sup>, Owen Vickery<sup>3,4</sup>, Amy Muellbauer<sup>1</sup>, Holly Monkhouse<sup>1</sup>, Thomas Griffiths<sup>1</sup>, Rory Hennell James<sup>1</sup>, Ben C. Berks<sup>3</sup>, James W. Coulton<sup>5,6</sup>, Phillip J. Stansfeld<sup>3,4</sup> & Susan M. Lea<sup>1,2,\*</sup>

1. Sir William Dunn School of Pathology, University of Oxford, South Parks Road, Oxford OX1 3RE, UK
2. Central Oxford Structural Molecular Imaging Centre, University of Oxford, South Parks Road, Oxford, OX1 3RE, UK
3. Department of Biochemistry, University of Oxford, South Parks Road, Oxford OX1 3QU
4. School of Life Sciences & Department of Chemistry, University of Warwick, Coventry, CV4 7AL, UK.
5. Department of Microbiology and Immunology, McGill University, 3775 University Street, Montreal, H3A 2B4, Canada
6. Département de biochimie et médecine moléculaire, Université de Montréal, 2900 boulevard Édouard-Montpetit, Montréal, H3T 1J4, Canada

\*For correspondence and requests for reagents: [susan.lea@path.ox.ac.uk](mailto:susan.lea@path.ox.ac.uk)

### Abstract

The bacterial flagellum is the proto-typical protein nanomachine and comprises a rotating helical propeller attached to a membrane-embedded motor complex. The motor consists of a central rotor surrounded by stator units that couple ion flow across the cytoplasmic membrane to torque generation. Here we present the structures of stator complexes from *Clostridium sporogenes*, *Bacillus subtilis* and *Vibrio mimicus*, allowing interpretation of the extensive body of data on stator mechanism. The structures reveal an unexpected asymmetric A<sub>5</sub>B<sub>2</sub> subunit assembly in which the five A subunits enclose the two B subunits. Comparison to structures of other ion-driven motors indicates that this A<sub>5</sub>B<sub>2</sub> architecture is fundamental to bacterial systems that couple energy from ion-flow to generate

mechanical work at a distance, and suggests that such events involve rotation in the motor structures.

## Introduction

A motor is a machine that supplies motive power for a device with moving parts. Biological systems use both linear and rotary motors to generate a variety of outputs. One of the most fascinating and complex biological rotary motors is the flagellar apparatus used by bacteria to propel themselves through fluid environments<sup>1</sup>. Although bacterial swimming was first observed in the 17<sup>th</sup> century<sup>2</sup>, a mechanistic understanding of how the bacterial flagellum generates rotation is still lacking. The core of the flagellum is a highly conserved motor (Fig. 1a) consisting of a cytoplasmic-membrane embedded rotor complex surrounded by varying numbers of stator complexes that generate torque<sup>3</sup>. While high resolution information has been available for monomeric components of the cytoplasmic portion of the rotor<sup>4</sup>, and has recently been obtained for the intact membrane-tethered rotor complex<sup>5</sup>, structural detail of the stators has thus far been limited to modelling studies<sup>6</sup>.

Stators harvest energy from either H<sup>+</sup> or Na<sup>+</sup> ion flow across the cytoplasmic membrane, generating torque in the cytoplasmic portion (C-ring) of the rotor complex<sup>7, 8, 9, 10</sup>. Chimeras between H<sup>+</sup>- and Na<sup>+</sup>-dependent stators are functional, implying that the mechanism converting ion flow into work is the same for the two coupling ions<sup>11</sup>. Stator complexes are built from two cytoplasmic membrane proteins, which for simplicity are generically referred to here as MotA and MotB. MotA is predicted to contain four transmembrane helices (TMH) with a large cytoplasmic insertion between TMH2 and TMH3. MotB is predicted to contain a short cytoplasmic sequence, a single TMH, and a C-terminal peptidoglycan binding (PGB) domain. Early biochemical work defined the stator complex

stoichiometry as MotA<sub>4</sub>B<sub>2</sub><sup>12</sup>, and this subunit composition has informed attempts to derive mechanism for conversion of ion flow into rotation (reviewed in <sup>13</sup>). Extensive experimental studies have led to a model of stator complex function in which docking of the MotA cytoplasmic loop to the rotor C-ring simultaneously induces ion permeation through the stator complex and release of the MotB-PGB domain to bind to the peptidoglycan (PG) surrounding the flagellar basal body<sup>14, 15</sup>. Ion flow is proposed to lead to conformational changes in the cytoplasmic domain of MotA that generate torque in the rotor<sup>16, 17, 18</sup>. In the absence of a stator complex structure various mechanistic hypotheses have been proposed to explain the coupling of ion flow to conformational change, most of which explicitly use the predicted 2-fold symmetry of a MotA<sub>4</sub>B<sub>2</sub> complex<sup>18, 19, 20</sup>.

## Results

### Flagellar stator complexes are MotA<sub>5</sub>B<sub>2</sub> complexes

We used cryo-electron microscopy (cryo-EM) to study stator complexes from a range of bacterial species with different ion specificities (Extended Data Fig. 1). Two-dimensional class averages of the complexes from three species (*Vibrio mimicus*, *Clostridium sporogenes* and *Bacillus subtilis*) clearly showed a distorted, pentagonal, structure (Fig. 1b). 3D reconstructions of these complexes yielded volumes that could only be interpreted as MotA<sub>5</sub>B<sub>2</sub> assemblies (Fig. 1c; Extended Data Fig. 2; Table 1), with five copies of MotA fully enclosing the TMHs of two copies of MotB (Fig. 2a). Although we do not observe the PGB-domains of MotB in the resolved structures, these domains must be present in the imaged complexes because the stator complexes were purified using an affinity tag located after the PGB domain. Thus, the PGB-domain of MotB has no fixed location with respect to the core complex in the context of the isolated protein. The stator complex structures are compatible

with sequence conservation data, with inter- and intra-molecular co-evolution data, and with published cysteine crosslinking<sup>21, 22</sup> and tryptophan scanning mutagenesis<sup>23, 24</sup> (Extended Data Fig. 3).

The four TMHs of MotA are arranged in two layers. TMH3 and TMH4 line the central pore, while TMH1 and TMH2 form a surrounding outer layer of helices (Fig. 2a,b). TMH1 and TMH2 are not in contact with each other within a single subunit but instead interact between adjacent subunits, thereby stabilising the MotA assembly. Immediately following TMH2 there is an amphipathic helix (AMPH) running perpendicular to the TMHs at the cytoplasmic membrane surface, with the five copies of this helix forming a belt around the outside of the structure. TMH3 and TMH4 extend 30 Å outside the membrane to form the core of the MotA cytoplasmic domain, with the rest of the domain built from helices inserted in the loop between the AMPH and TMH3. Both within and outside the membrane domain the pentameric arrangement of MotA is distorted (Fig. 2c). Charged residues shown to be essential for the interaction of the stator complex with the rotor C-ring<sup>25</sup> are located towards the base of this domain, forming a ring that decorates the surface of the pentamer (Extended Data Fig. 4).

The TMHs of the two copies of MotB are located in the central pore of the distorted MotA pentamer, with their hydrophobic sidechains completely buried within the MotA ring. From the N-terminal ends of the MotB TMHs clear densities extend down to contact the inner surfaces of TMH3 and TMH4 in the cytoplasmic domains of MotA (Fig. 3a,b; Extended Data Fig. 5a,b). Although the densities are too weak for the sequence to be traced, they are of sufficient length to account for most of the MotB N terminus, including a cluster of positive charges essential for motor function<sup>26</sup>. At the non-cytoplasmic face of the complex the MotB

TMHs emerge vertically from the MotA pentamer and are followed by another short helical section that packs down between the TMH3-TMH4 loops of the MotA chains (Fig. 3a,b; Extended Data Fig. 5a,b). The connectivity of these densities defines them as the plug helices previously implicated by mutagenesis as critical to sealing the complexes in an off state<sup>27</sup>.

Prior mutagenesis studies have established that a series of conserved residues in the TMHs of MotA and MotB are important for flagellar motion and/or ion-flow through the stator (reviewed in <sup>3</sup>). Invariant MotB<sub>D32</sub> (using the *Escherichia coli* numbering system) is the key protonatable residue and both copies are seen to lie within a ring formed by the five copies of another invariant polar residue, MotA<sub>T209</sub> (Fig. 3c, Extended Data Fig. 6). A second Thr residue (at a position corresponding to residue A180 in *E. coli* MotA) that is conserved in the Na<sup>+</sup>-dependent stators also contributes to this ring, and forms part of a track of Na<sup>+</sup>/H<sup>+</sup> specificity determining residues that line the inner surface of the MotA pore (Extended Data Fig. 1). Two conserved Pro residues in MotA have been shown to be important for torque generation<sup>28</sup>. One of these, MotA<sub>P222</sub> can now be seen to be required for contacts between neighbouring MotA monomers. The other, MotA<sub>P173</sub>, forms a second ring of conserved residues with MotA<sub>Y217</sub>, two helical turns down from the Thr ring. This hydrophobic ring contacts MotB at the completely conserved MotB<sub>W26</sub>. A MotB<sub>W26A</sub> substitution completely abolished motility confirming the importance of this contact (Fig. 3d).

### **Asymmetry and the implications for activation of ion flow**

The 5:2 stoichiometry of the stator complex leads to multiple levels of asymmetry in the structure (Fig. 2c; Extended Data Fig. 5c). The pentagon formed by the MotA subunits within the membrane is distorted to accommodate and seal around the two MotB TMHs. The asymmetry of this part of the complex is also driven by the two MotB plug helices sitting

between the MotA loops, which divide the MotA chains into two groups separated in the extracytoplasmic region. Removal of the MotB plug has been shown to lead to uncontrolled ion flow through the MotAB channel<sup>27</sup>. However, our structures show that the plug helices are not the sole block to ion permeation since there are no detectable channels across the cytoplasmic membrane compartment (Fig. 3e; Extended Data Fig. 5d). Embedding plug-free structures in full lipid bilayer models and running extended simulations demonstrated the observed structures are stable, low energy, states (Extended Data Fig. 7). No ion permeation across the bilayer was seen in any simulation, supporting the idea that the complexes currently seen will require rearrangement for activity.

Activation of ion flow is proposed to be triggered by docking of the inactive stator complex onto the flagellar C-ring via the MotA cytoplasmic domains resulting in signal propagation from the cytoplasm to the plug region and plug release<sup>14, 15</sup>. Our structures reveal two potential routes for such a signal. The first involves the cytoplasmic N-termini of the MotB subunits which contain functionally essential residues<sup>26</sup> that interact with the inside of the MotA pentamer through highly evolutionarily coupled contacts (Extended Data Fig. 3d). C-ring-induced movement of MotA would be communicated to MotB at this site leading to alterations at the opposite end of the MotB TMHs. The second possible route of signal propagation is directly through the MotA subunits, whereby hinging of the long TMH3 and TMH4 helices could alter the conformation of the plug helix binding loops to allow plug release. Our structures provide insight into how such a conformational change could occur, as we observe differing degrees of hinging of the MotA cytoplasmic domains relative to the membrane embedded helices (Fig. 3f; Extended Data Fig. 5e). Our structures also reveal that the two MotA residues known to be essential for interaction with the C-ring protein FliG<sup>25</sup> are located on opposite sides of the MotA cytoplasmic domain, with MotA<sub>R90</sub> from one copy

facing MotA<sub>E98</sub> from the neighbouring copy (Extended Data Fig. 4). Therefore docking of the C-terminal domain of FliG between two MotA subunits could trigger conformational change in the stator complex, consistent with earlier observations based on proteolytic sensitivity of MotA<sup>17</sup>.

### **Coupling of ion-flow to flagellar rotation**

The most striking feature of the asymmetry of the 5:2 subunit stoichiometry is that it places the TMHs of the two copies of MotB, including the critical MotB<sub>D32</sub> residue, in different environments within the distorted MotA pentagon (Extended Data Figure 6). The system therefore appears primed for differential binding of H<sup>+</sup> or Na<sup>+</sup> at the critical MotB<sub>D32</sub> residue to induce changes in the relative positioning of the MotB and MotA helices. As MotB becomes tethered to the PG upon stator complex activation<sup>14</sup> (Fig. 4a), this model would predict that the MotA ring moves around the MotB dimer. The 5:2 subunit stoichiometry is consistent with a model in which the two MotB<sub>D32</sub> residues alternate in terms of counter-ion occupancy and MotA binding mode. The coordination of ion binding to one MotB<sub>D32</sub> with the simultaneous release from the other allows for a processive model of stepping, whereby opening of one channel triggers rotation of the MotA ring by ~36° (Fig. 4b). This motion would bring the second MotB chain into the same position relative to the surrounding MotA subunits as the starting arrangement of the first MotB chain, thereby closing the first channel and opening the second. This model has the appeal that each subsequent ion binding event would be identical at a molecular level and trigger a further ratchet motion of 36°, with each turn of the MotA cytoplasmic domains providing a “power stroke” to the rotor. This model would impart unidirectional rotation to the MotA pentamer, and ten ion binding events would be required for a full 360° rotation. An alternative model, whereby ions binding sequentially to

each MotB trigger first a 36° rotation and then a reset to the original position, would also be compatible with the structure. Such a model would act as a ratchet, only providing a “power stroke” for every other binding event, and hence require twice as many ions as the unidirectional model for an equivalent movement of MotA. Although the stator complex would not undergo full rotation in this alternate model, it would still be capable of driving full rotation of the rotor component, acting like an energised escapement mechanism. Whether the “power stroke” mechanism in either model also involves conformational change centred on MotA<sub>P173</sub>, as has previously been proposed based on modelling studies, remains to be tested<sup>18</sup>. We note that the different conformations of MotA observed in our complexes do hinge around the location of MotA<sub>P173</sub> and the rotation mechanisms proposed would lead to each MotA altering conformation as it rotates around the MotBs. However, we also note that although MotA<sub>P173</sub> is completely conserved, it can be substituted with non-Pro residues without destroying function<sup>28</sup>.

Any mechanism for coupling ion flow to flagellar rotation must also explain how the direction of rotation of the flagellum can reverse in response to chemotactic stimuli. All experimental evidence (reviewed in <sup>29</sup>) shows that the chemotaxis machinery leads to changes in the FliG subunit of the C-ring rather than the stator complex. A unidirectional rotation model for the stator complex mechanism can account for flagellar reversal if the chemotaxis-linked conformational changes induced in the C-ring lead to an alteration in the side of the stator complex that is driving the rotation (Fig. 4c). Consistent with this proposal, large conformational changes in the stator-interacting FliG component of the C-ring have been observed in crystal structures of FliG fragments<sup>30</sup> and in recent cryo-electron tomographic maps <sup>31</sup>. This model also predicts that any reversal of the ion flow through the stator complex would have the potential to reverse the direction of flagellar rotation even in



the absence of switching by the chemotaxis machinery, and this phenomenon has been observed in *Streptococcus* species assayed under high pH conditions<sup>32, 33</sup>. Alternatively, the oscillating ratchet mechanism would be able to operate in reverse by remodelling of the C-ring to change the direction of the cog-wheel teeth.

### **Common architecture across multiple bacterial ion-driven machines**

The MotAB system is related at the sequence level to the ExbBD complex found in Gram-negative bacteria that uses ion-flow across the cytoplasmic membrane to power transport processes at the outer membrane via the trans-periplasmic TonB protein<sup>34</sup>. We determined cryo-EM structures of ExbBD complexes from *E. coli* and *Pseudomonas savastanoi* (Extended Data Fig. 8; Table 1). Both displayed a 5:2 ExbB:ExbD stoichiometry that differs from the subunit composition of earlier structures<sup>35, 36</sup>, but agrees with the subunit stoichiometry of a structure of the *E. coli* ExbBD reported whilst this manuscript was in preparation<sup>37</sup>. Comparison of these recent ExbB<sub>5</sub>D<sub>2</sub> structures to the stator complexes reveals a high level of structural conservation, particularly within the membrane domain (Extended Data Fig. 9a,b). Both the flattened pentagon geometry and the alignment of mechanistically important residues, such as the conserved Asp within a ring of Thr residues, suggest that the two systems use the same molecular mechanism. We therefore predict that the ExbB will rotate relative to the ExbD helices in response to proton flow. Outside the core TMH region there are structural differences between the systems that presumably reflect their very different biologies. ExbB is very differently elaborated relative to MotA, with only one TMH packing across the pair of helices that form the core inner ring and no bracing helices strengthening packing between subunits (Extended Data Fig. 9c). The ExbB cytoplasmic domains are only

superficially similar to the corresponding MotA domain and lack the short pair of C-terminal helices found in MotA (Extended Data Fig. 9d).

*P. savastanoi* ExbB and ExbD were purified as a complex with TonB when all three proteins were co-expressed (Extended Data Fig. 10a). However, no extra density, at a comparable level to the ExbBD components, was observed in the cryo-EM maps of this complex relative to the ExbBD complex alone, suggesting that TonB is located on the outside of the ExbBD complex and dissociates upon sample freezing. A peripheral location for TonB is consistent with both co-evolution analysis (Extended Data Fig. 10b) and mutagenesis/suppressor data<sup>38</sup>, which suggest that the TonB binding site is on the outside of the ExbB transmembrane domain (Extended Data Fig. 10b). TonB consists of a single pass TMH, followed by an extended periplasmic region that interacts with the periplasmic domain of ExbD<sup>39</sup>, and terminates in a folded domain that links with outer-membrane receptor proteins<sup>40</sup>. We speculate that the TonB TMH packs against the exterior of the ExbBD complex so that conformational change in TonB is driven by rotation of the ExbB component relative to ExbD. In further support of this hypothesis we note that, at a low contour level, a single additional density that we assign as the TonB TMH is seen to traverse the micelle on the exterior of the ExbBD complex (Extended Data Fig. 10c) packing against ExbB, in the location predicted by analysis of co-variance (Extended Data Fig. 10b). By extension, the homologous TolQRA system will also share this architecture and be mechanistically related<sup>41</sup>.

## Discussion

The structures presented in this study demonstrate an asymmetric 5:2 stoichiometry for the MotA:MotB flagellar stator complex, in contrast to the previously proposed symmetric 4:2 models. This study also corroborates a recently observed 5:2 stoichiometry of the

ExbB:ExbD motor component of the Ton transport system. A picture therefore emerges of the likely mechanistic importance of this shared stoichiometry for motor function. This link is further strengthened by another observation of this stoichiometry in an unrelated bacterial motor complex, the structure of which is described in a companion paper<sup>42</sup>. Bacteria from the *Bacteroidetes* phylum possess a two-component motor complex in the cytoplasmic membrane that harvests energy from ion-flow to drive protein secretion and to power bacterial motility via a non-flagellar mechanism termed gliding motility<sup>43</sup>. Although the constituent GldL and GldM subunits of this motor have no sequence similarity to the subunits of the MotAB or ExbBD complexes, the *Bacteroidetes* motor complex exhibits the same 5:2 subunit stoichiometry as these complexes (Fig. 5a). All three complexes have an intramembrane core consisting of a central subunit TMH dimer surrounded by a 10 TMH ring. Structural comparisons demonstrate the similarity between the three motors in the arrangement of this intramembrane core and of the height within the membrane at which charged residues critical to function are located (Fig. 5b,c).

Such shared underlying architecture between otherwise highly dissimilar motors (Fig. 5d) implies an unexpected commonality in their mechanism. Analysis of the structural asymmetry at the heart of the complexes strongly implies that this common mechanism involves processive rotation of the dimeric component relative to the pentameric component in response to the sequential binding of ions to the complex. The relatively simple core machinery in the membrane provides a template onto which elaborations can be built to provide specific biological function. This allows for a remarkable degree of adaptation, and introduces means by which either component could be tethered to a cellular structure in order to drive rotation of the other component; for example tethering of the dimer to the peptidoglycan in the case of the flagellar stator complexes, or the proposed tethering of the

pentamer in the *Bacteroidetes* motor. This work paves the way for future studies analysing the ubiquity of these mechanisms across the systems discussed here and potentially related motors with different biological roles in other bacterial species.

## **Acknowledgements**

We thank David Blair for providing *E. coli* RP6894. We thank E. Johnson and A. Costin of the Central Oxford Structural Molecular Imaging Centre (COSMIC) for assistance with data collection, and H. Elmlund (Monash) for access to SIMPLE3.0 code ahead of release. We acknowledge the use of the Central Oxford Structural Microscopy and Imaging Centre (COSMIC). The Central Oxford Structural Microscopy and Imaging Centre is supported by the Wellcome Trust (grant no. 201536), The EPA Cephalosporin Trust, The Wolfson Foundation and a Royal Society/Wolfson Foundation Laboratory Refurbishment Grant (no. WL160052). Research in S.M.L.'s laboratory is supported by a Wellcome Trust Investigator Award (grant no. 100298), a Collaborative award (no. 209194) and a Medical Research Council (London) Programme Grant (no. MR/M011984/1). Research in B.C.B.'s laboratory is supported by a Wellcome Trust Investigator Award (grant no. 107929/Z/15/Z). Research in J.W.C.'s laboratory is supported by the Canadian Institutes of Health Research (grant 178048-BMA-CFAA-11449). Research in P.J.S.'s lab is funded by Wellcome (208361/Z/17/Z), the MRC (MR/S009213/1) and BBSRC (BB/P01948X/1, BB/R002517/1 and BB/S003339/1). This project made use of time on ARCHER and JADE granted via the UK High-End Computing Consortium for Biomolecular Simulation, HECBioSim (<http://hecbiosim.ac.uk>), supported by EPSRC (grant no. EP/R029407/1), and Athena at HPC Midlands+, which was funded by the EPSRC on grant EP/P020232/1, and used the University of Warwick Scientific Computing Research Technology Platform for computational access.

## Author contributions

J.C.D carried out all biochemical work except as credited otherwise, prepared cryo-EM grids, collected and processed EM data and determined the structures. J.C.D., S.J., and S.M.L designed the project, interpreted the data, built models, and wrote the first draft of the paper. S.J. also performed MALS experiments. O.V. and P.J.S. performed molecular dynamics simulations. A.M., H.M., and T.G. carried out biochemical work on *Pseudomonas* TonB-ExbB-ExbD. R.H.J. and B.C.B. contributed the GldLM structure. J.W.C. initiated and provided materials for the ExbBD project. All authors commented on drafts of the manuscript. Correspondence and requests for material should be addressed to S.M.L. ([susan.lea@path.ox.ac.uk](mailto:susan.lea@path.ox.ac.uk)).

## Declaration of Interests

The authors declare no competing interests.

## Methods

### Bacterial strains and plasmids

Bacterial strains and plasmids used in this study are listed in Supplementary Table 1. The pT12 backbone used for all protein expression was derived from Kuhlen *et al.*<sup>44</sup>. Plasmids were generated by Gibson assembly of PCR fragments using the NEBuilder HiFi Master Mix (NEB). Fragments were created by PCR with the relevant primers (listed in Supplementary Table 2) using Q5 polymerase (NEB) and genomic DNA templates obtained from the Leibniz Institute [dsmz.de]: *Vibrio mimicus* (DSM 19130), *Bacillus subtilis* 168 (DSM 402), *Clostridium sporogenes* 388 (DSM 795), *Escherichia coli* W (DSM 1116), *Pseudomonas savastanoi*, pv.

phaseolicola 1448A (DSM 21482). Gibson assembly and PCR were carried out following the manufacturer's recommendations. *E. coli* RP6894 ( $\Delta$ *motAB*) for motility assays was generated by J. S. Parkinson and gifted by D.F. Blair.

### **Purification of MotAB/PomAB and ExbBD complexes**

*V. mimicus* PomAB, its derivative PomAB $_{\Delta 61-120}$  lacking unstructured periplasmic residues of PomB, *B. subtilis* MotAB, *C. sporogenes* MotAB, *E. coli* ExbBD, and *P. savastanoi* TonB-ExbBD complexes were expressed in *E. coli* MT56 as a single operon from a pT12 vector encoding a C-terminal twin-strep tag. Purification steps were similar across all constructs and carried out at 4 °C. Briefly, cells were grown at 37 °C for 16 h in TB media containing kanamycin (50 µg/mL) and rhamnose monohydrate (0.1% w/v) then collected by centrifugation at 4,000*g*. Cell pellets were resuspended in TBS (100 mM Tris, 150 mM NaCl, 1 mM EDTA pH 8.0) plus 30 µg/mL DNase I and 400 µg/mL lysozyme for 30 mins before passage through an EmulsiFlex C5 homogenizer (Avestin) at 15,000 psi. Unbroken cells were removed by centrifugation at 24,000*g* for 20 min. The supernatant was recovered and total membranes were collected by centrifugation at 200,000*g* for 1.5 h. Membranes were resuspended in TBS and solubilized by incubation with 1% (w/v) lauryl maltose neopentyl glycol (LMNG; Anatrace) for 2 h. Insoluble material was removed by centrifugation at 100,000*g* for 30 min. Solubilized membranes were then applied to a Streptactin XT column (IBA Lifesciences). The resin was washed with 10 column volumes (CV) of TBS containing 0.02% (w/v) LMNG and proteins were eluted in 5 CV of TBS supplemented with 0.01% (w/v) LMNG and 50 mM D-biotin (IBA Lifesciences). Eluates were concentrated using a 100-kDa molecular weight cutoff (MWCO) Vivaspın 6 (GE Healthcare) centrifugal filter unit and injected onto a Superose 6 Increase 10/300 GL size exclusion column (GE Healthcare) pre-

equilibrated in TBS plus 0.01% (w/v) LMNG. Peak fractions were collected and concentrated using a 100-kDa MWCO Vivaspın 500 (GE Healthcare) centrifugal filter unit (Supplementary Figure 1 & Extended Data Fig. 10).

For *P. savastanoi* TonB-ExbBD and ExbBD complexes, SEC-MALS analysis was carried out by injecting 100  $\mu$ L ( $A_{280\text{nm}} = 1.0$ ) of either sample onto a Superose 6 increase 10/300 GL (GE Healthcare) equilibrated in TBS containing 0.02% (w/v) LMNG. Light scattering and refractive index changes were measured using a Dawn Heleos-II light-scattering detector and an Optilab-TrEX refractive index monitor. Analysis was carried out using ASTRA 6.1.1.17 software using a theoretical extinction coefficient of 1.02 ( $\text{Abs}_{0.1\%}$ ) and a protein  $\text{dn}/\text{dc}$  value of 0.186 mL/g and a detergent  $\text{dn}/\text{dc}$  value of 0.143 mL/g (Extended Data Fig. 10).

### **Cryo-EM sample preparation and imaging**

Purified complexes (4  $\mu$ L each) of *V. mimicus* PomAB ( $A_{280\text{nm}} = 0.5$ ), PomAB $_{\Delta 61-120}$  ( $A_{280\text{nm}} = 0.55$ ), *B. subtilis* MotAB ( $A_{280\text{nm}} = 1.0$ ), *C. sporogenes* MotAB ( $A_{280\text{nm}} = 0.8$ ), *E. coli* ExbBD ( $A_{280\text{nm}} = 3.2$ ), or *P. savastanoi* TonB-ExbBD ( $A_{280\text{nm}} = 2.0$ ) were adsorbed to glow-discharged holey carbon-coated grids (Quantifoil 300 mesh, Au R1.2/1.3) for 10 s. Grids were then blotted for 2 s at 100% humidity at 8°C and frozen in liquid ethane using a Vitrobot Mark IV (FEI). Alternatively, specimens were prepared by supplementing *V. mimicus* PomAB ( $A_{280\text{nm}} = 2.3$ ), PomAB $_{\Delta 61-120}$  ( $A_{280\text{nm}} = 3.7$ ), *B. subtilis* MotAB ( $A_{280\text{nm}} = 7.2$ ), *C. sporogenes* MotAB ( $A_{280\text{nm}} = 8.6$ ), *E. coli* ExbBD ( $A_{280\text{nm}} = 4.2$ ) with 0.7 mM fluorinated octyl maltoside (fluorinated OM; Anatrace) prior to grid preparation.

Data were collected in counting mode on a Titan Krios G3 (FEI) operating at 300 kV with a GIF energy filter (Gatan) and K2 Summit detector (Gatan) using a pixel size of 0.822 Å, a dose rate of 4.05 e<sup>-</sup>/pix/s, and an exposure of 8 s, corresponding to a total dose of 48 e<sup>-</sup>/Å<sup>2</sup>.

Movies were collected across 20 (*V. mimicus* PomAB and PomAB<sub>Δ61-120</sub> datasets) or 32 fractions (*B. subtilis* MotAB, *C. sporogenes* MotAB, *E. coli* ExbBD, and *P. savastanoi* ExbBD datasets). Except for *P. savastanoi* TonB-ExbBD, all datasets included movies from grids prepared with and without the presence of fluo OM to improve distribution of particle orientations. Example micrographs are shown in Supplementary Fig. 2.

### Cryo-EM data processing

Motion correction and dose weighting were performed using MotionCorr implemented in Relion 3.0<sup>45</sup>. Contrast transfer function parameters were estimated using CTFFIND4<sup>46</sup>. Particles were picked in Simple<sup>47</sup> and subsequent processing was all carried out in Relion 3.0<sup>45</sup>. Gold standard Fourier shell correlations using the 0.143 criterion and local resolution estimations were calculated within Relion<sup>45</sup> (Extended Data Fig. 2).

*V. mimicus* PomAB particles (1,172,445) underwent one round of reference-free 2D classification, from which 253,681 particles were selected and used to generate an *ab initio* initial model. This model was low-pass filtered to 30 Å and used as reference for 3D classification, generating a class that refined to 6.8 Å from 155,280 particles.

For the deletion construct PomAB<sub>Δ61-120</sub> that improved particle orientations and data quality, particles (2,383,062) were extracted from 13,980 movies. Following one round of reference-free 2D classification, 800,844 particles were classified in 3D (4 classes) against a 40 Å low-pass filtered map of PomAB. A class containing 244,654 particles was further subjected to masked refinement yielding a 4.8 Å map. Refinement after Bayesian particle polishing and per-particle defocus with beamtilt estimation further improved map quality to 4.2 Å (Supplementary Fig. 3).



*B. subtilis* MotAB particles (1,532,430) were extracted over 11,588 movies. After 2D classification, selected particles (397,584) underwent two rounds of 3D classification (3 classes each) using a 40 Å low-pass filtered map generated from a subset of particles refined against a 60 Å low-pass filtered map of PomAB<sub>Δ61-120</sub>. A class made up of 122,615 particles was refined to 3.9 Å. Bayesian particle polishing further improved map resolution by 0.2 Å, and subsequent CTF refinement using per-particle defocus with beamtilt estimation generated a 3.5 Å map (Supplementary Fig. 4). To improve MotB N-terminal and plug densities, a subset of fluorinated particles (43,375) was selected and refined against the 3.5 Å reconstruction, generating a 5.0 Å map that was used to depict these regions in Extended Data Fig. 5.

*C. sporogenes* MotAB particles (1,998,900) were extracted from 9,148 movies and subjected to a round of reference-free 2D classification. Initial 3D classification performed against a 60 Å low-pass filtered map of *B. subtilis* MotAB revealed two prominent classes which represented a monomeric MotAB complex and a non-physiological end-to-end dimer of MotAB. These classes were used as references in a supervised multi-reference 3D classification against the full 1,137,357 particle set to exclude dimeric particles. Unsupervised 3D classification (4 classes) performed against 865,446 monomeric particles and further refinement yielded 3.8 Å from 314,230 particles. Bayesian particle polishing followed by per-particle defocus with beamtilt estimation further improved map quality to 3.4 Å (Supplementary Fig. 5).

Movies (6,902) were collected for *E. coli* ExbBD, resulting in the extraction of 2,045,350 particles. Following one round of reference-free 2D classification, an initial model of ExbBD was generated by 3D classification and refinement of a particle subset against a 40 Å low-pass filtered 5:1 ExbBD complex<sup>36</sup> (EMD-6928). The resulting map was used as initial

model for multiple rounds of 3D classification against the full 2D-classified particle set (755,677). After refinement of 227,700 particles, this protocol generated a 5.8 Å map, improving to 4.6 Å following Bayesian particle polishing and per-particle defocus plus beamtilt estimation (Supplementary Fig. 6).

Movies (4,232) were collected for *P. savastanoi* TonB-ExbBD and 1,342,900 particles were extracted. Particles were subjected to two rounds of 2D classification with centered re-extraction between classifications. The cleaned 499,697 particles were subjected to C5-symmetric 3D classification against a low-pass filtered map previously generated from 3D classification and refinement (C1) of an earlier subset of particles against a 40 Å low-pass filtered map of our 5:2 *E. coli* ExbBD structure. The resultant 202,356 particles were refined with C5 symmetry to generate a 3.5 Å map that lacked density for the transmembrane helices (TMHs) of ExbD. Particles were polished and subjected to an additional round of 2D classification followed by 3D classification with C1 symmetry, resulting in 3.9 Å map from 110,164 particles after refinement in C1. An additional round of Bayesian polishing and per-particle defocus and beamtilt estimation followed by refinement (C1) yielded a 3.8 Å map. Alignment-free 3D classification and subsequent local refinement (C1) yielded a 3.8 Å map with improved density for the TMHs of ExbD from 65,617 particles (Supplementary Fig. 7).

Directional FSC and orientation distribution plots are provided in Supplementary Information (Supplementary Figs. 8 & 9 respectively).

### **Model building and refinement**

Atomic models were built using Coot<sup>48</sup>. Models were built only in the two volumes that allowed unambiguous docking of sequence into side chain density in the central pair of helices (MotAB *C. sporogenes* & *B. subtilis*). Multiple rounds of rebuilding (in both the globally

sharpened and local-resolution filtered maps) and real-space refinement in Phenix<sup>49</sup> using secondary structure, rotamer and Ramachandran restraints yielded the final models described in Table 1. All models were validated using Molprobity<sup>50</sup>. Conservation analysis was carried out using the Consurf server<sup>51</sup>. A homology model of *E. coli* MotAB was generated by sequence threading against the *Clostridium* model using Phyre2<sup>52</sup>. Figures were prepared using UCSF ChimeraX<sup>53</sup> and Pymol (The PyMOL Molecular Graphics System, Version 2.0 Schrödinger, LLC). All models depicted in figures are based on the highest resolution *Clostridium* model, unless otherwise specified. Residue numbering adopts the reference *E. coli* sequence and model; a residue conversion table is provided (Supplementary Table 3). Closeups of density for side chains shown in Fig. 3 are shown in Supplementary Fig. 10.

### Evolutionary covariance analysis

Coevolutionary contacts for *E. coli* W MotA were determined by the Gremlin web-server<sup>6</sup>. Searches used the Jackhmmer algorithm for multiple sequence alignment, an E-value threshold of  $10^{-10}$  and a minimum coverage of 75%. Intra- and intermolecular contacts were mapped to the *E. coli* MotA structure using Gremlin beta<sup>6</sup>. Intermolecular contacts between MotA and MotB (residues 1-120) were determined using an E-value threshold of  $10^{-20}$  and  $10^{-2}$ , respectively. Intermolecular contacts between TonB and ExbB were determined using an E-value threshold of  $10^{-20}$ . Contacts with a probability score greater than 0.9 were regarded as significant and listed in Supplementary Table 4.

### Simulation setup

All simulations were run using GROMACS 2018<sup>54</sup>. The systems were initially setup using the Martini 2.2 coarse-grain (CG) force field and solvated with water and 0.15 M NaCl

to neutralise the system<sup>55</sup>. The membranes were constructed using INSANE with a 4:1 ratio of POPE:POPG lipids<sup>56</sup>. An elastic network of  $1000 \text{ kJ mol}^{-1} \text{ nm}^{-2}$  was applied between all backbone beads between 0.5 and 1 nm. Electrostatics were described using the reaction field method, with a cut-off of 1.1 nm using the potential shift modifier and the van der Waals interactions were shifted between 0.9-1.1 nm. The systems were first energy minimised by steepest descent algorithm to  $1000 \text{ kJ mol}^{-1} \text{ nm}^{-1}$  and then simulated for a total of 1  $\mu\text{s}$ . The temperature and pressure were kept constant throughout the simulation at 310 K and 1 bar respectively, with protein, lipids and water/ions coupled individually to a temperature bath by the V-rescale method<sup>57</sup> and a semi-isotropic Parrinello-Rahman barostat<sup>58</sup>. The final snapshots from the CG simulations were then converted back to an atomistic description using CG2AT<sup>59</sup>.

### Atomistic simulations

The charged N- and C- termini of the converted protein were capped using acetyl and methyl moieties, respectively. All ionisable groups were simulated with default protonation states, unless otherwise mentioned. The virtual site model for hydrogen atoms<sup>60</sup>, adapted for the charmm36 forcefield<sup>61</sup> was employed, allowing the use of a 4 fs timestep during the simulations. Electrostatics were described using PME, with a cut-off of 1.2 nm and the van der Waals interactions were shifted between 1-1.2 nm. The tip3p water model was used, the water bond angles and distances were constrained by SETTLE<sup>62</sup>. All other bonds were constrained using the LINCS algorithm<sup>63</sup>. The systems were then equilibrated for a further 1 ns using a 4 fs timestep with positional restraints of  $1000 \text{ kJ mol}^{-1} \text{ nm}^{-2}$  on the heavy atoms, in a NPT ensemble with temperature V-rescale coupling at 310 K<sup>57</sup> and semi-isotropic Parrinello-Rahman barostat at 1 bar with protein, lipids and water/ions coupled individually<sup>58</sup>.

The Production simulations were performed without position restraints for a total of 200 ns and were run in triplicate.

### **Motility assay**

*E. coli* RP6894 ( $\Delta$ *motAB*) was transformed with pT12-derived plasmids encoding C-terminal twin-strep tagged MotAB containing point mutations or appropriate controls. Saturated overnight cultures (2  $\mu$ L) were injected into soft agar plates (0.3% w/v agar in tryptone broth) containing kanamycin (30  $\mu$ g/mL) plus rhamnose monohydrate (0.5% w/v) and incubated in a humidified chamber for 23 h at 25 °C.

### **Pulldowns**

*E. coli* RP6894 ( $\Delta$ *motAB*) or MT56 were transformed with pT12-derived plasmids encoding C-terminal twin-strep tagged MotAB containing the specified point mutations. Cultures were grown at 37 °C for 16 h in terrific broth containing kanamycin (50  $\mu$ g/mL) and rhamnose monohydrate (0.1% w/v). Normalized cell counts were lysed by resuspension in 200 mM Tris pH 8.0, 300 mM NaCl, 2 mM EDTA plus 30  $\mu$ g/mL DNase I and 400  $\mu$ g/mL lysozyme for 30 min then solubilized in 1.5 % w/v LMNG for 1 h. Insoluble material was removed by centrifugation at 18,000 x g for 30 min. LMNG-solubilized lysates were added to TBS-prewashed MagStrep XT magnetic beads (IBA Lifesciences) for 1 h with mild shaking. Beads were isolated and washed twice with TBS plus 0.025% w/v LMNG followed by elution with TBS plus 0.025% w/v LMNG and 50 mM D-biotin. Eluates were diluted in SDS-PAGE sample buffer and run on a 4–20% polyacrylamide gel (NuSep), followed by staining with InstantBlue (Expedeon). Assays were performed in duplicate. Results are shown in Supplementary Figure 11.

### **Data availability**

The data that support the findings of this study are available from the corresponding author upon reasonable request. Cryo-EM volumes and atomic models have been deposited to the EMDB (accession codes EMD-10895, EMD-10899, EMD-10901, EMD-10902, EMD-10897) and PDB (accession codes 6YSF and 6YSL), respectively.

## References

1. Berg, H.C. The rotary motor of bacterial flagella. *Annual review of biochemistry* **72**, 19-54 (2003).
2. Leeuwenhoek, A. Observation, communicated to the publisher by Mr Anthony van Leewenhoek, in a Dutch letter of the 9 Octob. 1676 here English'd: concerning little animals by him observed in rain-well-sea and snow water; as also in water wherein pepper had lain infused. *Phil. Trans.* **12**, 821-831 (1677).
3. Nakamura, S. & Minamino, T. Flagella-Driven Motility of Bacteria. *Biomolecules* **9** (2019).
4. Lee, L.K., Ginsburg, M.A., Crovace, C., Donohoe, M. & Stock, D. Structure of the torque ring of the flagellar motor and the molecular basis for rotational switching. *Nature* **466**, 996-1000 (2010).
5. Johnson, S. *et al.* Symmetry mismatch in the MS-ring of the bacterial flagellar rotor explains the structural coordination of secretion and rotation. *Nat Microbiol* (2020).
6. Ovchinnikov, S. *et al.* Large-scale determination of previously unsolved protein structures using evolutionary information. *Elife* **4**, e09248 (2015).
7. Kojima, S. Dynamism and regulation of the stator, the energy conversion complex of the bacterial flagellar motor. *Curr Opin Microbiol* **28**, 66-71 (2015).
8. Blair, D.F. & Berg, H.C. Restoration of torque in defective flagellar motors. *Science* **242**, 1678-1681 (1988).
9. Blair, D.F. & Berg, H.C. The MotA protein of E. coli is a proton-conducting component of the flagellar motor. *Cell* **60**, 439-449 (1990).
10. Larsen, S.H., Adler, J., Gargus, J.J. & Hogg, R.W. Chemomechanical coupling without ATP: the source of energy for motility and chemotaxis in bacteria. *Proc Natl Acad Sci U S A* **71**, 1239-1243 (1974).

11. Asai, Y., Yakushi, T., Kawagishi, I. & Homma, M. Ion-coupling determinants of Na<sup>+</sup>-driven and H<sup>+</sup>-driven flagellar motors. *J Mol Biol* **327**, 453-463 (2003).
12. Kojima, S. & Blair, D.F. Solubilization and purification of the MotA/MotB complex of *Escherichia coli*. *Biochemistry* **43**, 26-34 (2004).
13. Nirody, J.A., Sun, Y.-R. & Lo, C.-J. The biophysicist's guide to the bacterial flagellar motor. *Advances in Physics: X* **2**, 324-343 (2017).
14. Kojima, S. *et al.* The Helix Rearrangement in the Periplasmic Domain of the Flagellar Stator B Subunit Activates Peptidoglycan Binding and Ion Influx. *Structure* **26**, 590-598 e595 (2018).
15. Zhu, S. *et al.* Conformational change in the periplasmic region of the flagellar stator coupled with the assembly around the rotor. *Proc Natl Acad Sci U S A* **111**, 13523-13528 (2014).
16. Kim, E.A., Price-Carter, M., Carlquist, W.C. & Blair, D.F. Membrane segment organization in the stator complex of the flagellar motor: implications for proton flow and proton-induced conformational change. *Biochemistry* **47**, 11332-11339 (2008).
17. Kojima, S. & Blair, D.F. Conformational change in the stator of the bacterial flagellar motor. *Biochemistry* **40**, 13041-13050 (2001).
18. Mandadapu, K.K., Nirody, J.A., Berry, R.M. & Oster, G. Mechanics of torque generation in the bacterial flagellar motor. *Proc Natl Acad Sci U S A* **112**, E4381-4389 (2015).
19. Boschert, R., Adler, F.R. & Blair, D.F. Loose coupling in the bacterial flagellar motor. *Proc Natl Acad Sci U S A* **112**, 4755-4760 (2015).
20. Nishihara, Y. & Kitao, A. Gate-controlled proton diffusion and protonation-induced ratchet motion in the stator of the bacterial flagellar motor. *Proc Natl Acad Sci U S A* **112**, 7737-7742 (2015).
21. Braun, T.F., Al-Mawsawi, L.Q., Kojima, S. & Blair, D.F. Arrangement of core membrane segments in the MotA/MotB proton-channel complex of *Escherichia coli*. *Biochemistry* **43**, 35-45 (2004).
22. Braun, T.F. & Blair, D.F. Targeted disulfide cross-linking of the MotB protein of *Escherichia coli*: evidence for two H<sup>(+)</sup> channels in the stator Complex. *Biochemistry* **40**, 13051-13059 (2001).
23. Sharp, L.L., Zhou, J. & Blair, D.F. Features of MotA proton channel structure revealed by tryptophan-scanning mutagenesis. *Proc Natl Acad Sci U S A* **92**, 7946-7950 (1995).

24. Sharp, L.L., Zhou, J. & Blair, D.F. Tryptophan-scanning mutagenesis of MotB, an integral membrane protein essential for flagellar rotation in *Escherichia coli*. *Biochemistry* **34**, 9166-9171 (1995).
25. Yakushi, T., Yang, J., Fukuoka, H., Homma, M. & Blair, D.F. Roles of charged residues of rotor and stator in flagellar rotation: comparative study using H<sup>+</sup>-driven and Na<sup>+</sup>-driven motors in *Escherichia coli*. *J Bacteriol* **188**, 1466-1472 (2006).
26. Hosking, E.R. & Manson, M.D. Clusters of charged residues at the C terminus of MotA and N terminus of MotB are important for function of the *Escherichia coli* flagellar motor. *J Bacteriol* **190**, 5517-5521 (2008).
27. Hosking, E.R., Vogt, C., Bakker, E.P. & Manson, M.D. The *Escherichia coli* MotAB proton channel unplugged. *J Mol Biol* **364**, 921-937 (2006).
28. Braun, T.F. *et al.* Function of proline residues of MotA in torque generation by the flagellar motor of *Escherichia coli*. *J Bacteriol* **181**, 3542-3551 (1999).
29. Minamino, T., Kinoshita, M. & Namba, K. Directional Switching Mechanism of the Bacterial Flagellar Motor. *Comput Struct Biotechnol J* **17**, 1075-1081 (2019).
30. Lam, K.H. *et al.* Multiple conformations of the FliG C-terminal domain provide insight into flagellar motor switching. *Structure* **20**, 315-325 (2012).
31. Chang, Y. *et al.* Molecular mechanism for rotational switching of the bacterial flagellar motor. *BioRxiv* doi: <https://doi.org/10.1101/2020.05.18.101634> (2020).
32. Khan, S., Dapice, M. & Humayun, I. Energy transduction in the bacterial flagellar motor. Effects of load and pH. *Biophys J* **57**, 779-796 (1990).
33. Manson, M.D., Tedesco, P.M. & Berg, H.C. Energetics of flagellar rotation in bacteria. *J Mol Biol* **138**, 541-561 (1980).
34. Marmon, L. Elucidating the origin of the ExbBD components of the TonB system through Bayesian inference and maximum-likelihood phylogenies. *Mol Phylogenet Evol* **69**, 674-686 (2013).
35. Celia, H. *et al.* Structural insight into the role of the Ton complex in energy transduction. *Nature* **538**, 60-65 (2016).
36. Maki-Yonekura, S. *et al.* Hexameric and pentameric complexes of the ExbBD energizer in the Ton system. *Elife* **7** (2018).
37. Celia, H. *et al.* Cryo-EM structure of the bacterial Ton motor subcomplex ExbB-ExbD provides information on structure and stoichiometry. *Commun Biol* **2**, 358 (2019).



38. Swayne, C. & Postle, K. Taking the Escherichia coli TonB transmembrane domain "offline"? Nonprotonatable Asn substitutes fully for TonB His20. *J Bacteriol* **193**, 3693-3701 (2011).
39. Ollis, A.A., Kumar, A. & Postle, K. The ExbD periplasmic domain contains distinct functional regions for two stages in TonB energization. *J Bacteriol* **194**, 3069-3077 (2012).
40. Pawelek, P.D. *et al.* Structure of TonB in complex with FhuA, E. coli outer membrane receptor. *Science* **312**, 1399-1402 (2006).
41. Cascales, E., Lloubes, R. & Sturgis, J.N. The TolQ-TolR proteins energize TolA and share homologies with the flagellar motor proteins MotA-MotB. *Mol Microbiol* **42**, 795-807 (2001).
42. Hennell-James, R. *et al.* Structure of a proton-powered molecular motor that drives protein transport and gliding motility. *bioRxiv*, 2020.2005.2011.089193 (2020).
43. McBride, M.J. & Zhu, Y. Gliding motility and Por secretion system genes are widespread among members of the phylum bacteroidetes. *J Bacteriol* **195**, 270-278 (2013).
44. Kuhlen, L. *et al.* Structure of the core of the type III secretion system export apparatus. *Nature structural & molecular biology* **25**, 583-590 (2018).
45. Zivanov, J., Nakane, T. & Scheres, S.H.W. A Bayesian approach to beam-induced motion correction in cryo-EM single-particle analysis. *IUCr* **6**, 5-17 (2019).
46. Rohou, A. & Grigorieff, N. CTFFIND4: Fast and accurate defocus estimation from electron micrographs. *Journal of structural biology* **192**, 216-221 (2015).
47. Reboul, C.F., Eager, M., Elmlund, D. & Elmlund, H. Single-particle cryo-EM-Improved ab initio 3D reconstruction with SIMPLE/PRIME. *Protein science : a publication of the Protein Society* **27**, 51-61 (2018).
48. Brown, A. *et al.* Tools for macromolecular model building and refinement into electron cryo-microscopy reconstructions. *Acta crystallographica. Section D, Biological crystallography* **71**, 136-153 (2015).
49. Afonine, P.V. *et al.* Real-space refinement in PHENIX for cryo-EM and crystallography. *Acta crystallographica. Section D, Structural biology* **74**, 531-544 (2018).
50. Williams, C.J. *et al.* MolProbity: More and better reference data for improved all-atom structure validation. *Protein science : a publication of the Protein Society* **27**, 293-315 (2018).

51. Ashkenazy, H. *et al.* ConSurf 2016: an improved methodology to estimate and visualize evolutionary conservation in macromolecules. *Nucleic acids research* **44**, W344-350 (2016).
52. Kelley, L.A., Mezulis, S., Yates, C.M., Wass, M.N. & Sternberg, M.J. The Phyre2 web portal for protein modeling, prediction and analysis. *Nat Protoc* **10**, 845-858 (2015).
53. Goddard, T.D. *et al.* UCSF ChimeraX: Meeting modern challenges in visualization and analysis. *Protein science : a publication of the Protein Society* **27**, 14-25 (2018).
54. Abraham, M.J. *et al.* GROMACS: High performance molecular simulations through multi-level parallelism from laptops to supercomputers. *SoftwareX* **1-2**, 19-25 (2015).
55. de Jong, D.H. *et al.* Improved Parameters for the Martini Coarse-Grained Protein Force Field. *Journal of Chemical Theory and Computation* **9**, 687-697 (2012).
56. Wassenaar, T.A., Ingólfsson, H.I., Böckmann, R.A., Tieleman, D.P. & Marrink, S.J. Computational Lipidomics with insane: A Versatile Tool for Generating Custom Membranes for Molecular Simulations. *Journal of Chemical Theory and Computation* **11**, 2144-2155 (2015).
57. Bussi, G., Donadio, D. & Parrinello, M. Canonical sampling through velocity rescaling. *The Journal of Chemical Physics* **126** (2007).
58. Parrinello, M. & Rahman, A. Polymorphic transitions in single crystals: A new molecular dynamics method. *Journal of Applied Physics* **52**, 7182-7190 (1981).
59. Stansfeld, P.J. & Sansom, M.S.P. From Coarse Grained to Atomistic: A Serial Multiscale Approach to Membrane Protein Simulations. *Journal of Chemical Theory and Computation* **7**, 1157-1166 (2011).
60. Feenstra, K.A., Hess, B. & Berendsen, H.J.C. Improving efficiency of large time-scale molecular dynamics simulations of hydrogen-rich systems. *Journal of Computational Chemistry* **20**, 786-798 (1999).
61. Olesen, K., Awasthi, N., Bruhn, D.S., Pezeshkian, W. & Khandelia, H. Faster Simulations with a 5 fs Time Step for Lipids in the CHARMM Force Field. *Journal of Chemical Theory and Computation* **14**, 3342-3350 (2018).
62. Miyamoto, S. & Kollman, P.A. Settle: An analytical version of the SHAKE and RATTLE algorithm for rigid water models. *Journal of Computational Chemistry* **13**, 952-962 (1992).
63. Hess, B., Bekker, H., Berendsen, H.J.C. & Fraaije, J.G.E.M. LINCS: A linear constraint solver for molecular simulations. *Journal of Computational Chemistry* **18**, 1463-1472 (1997).





## Figure Legends

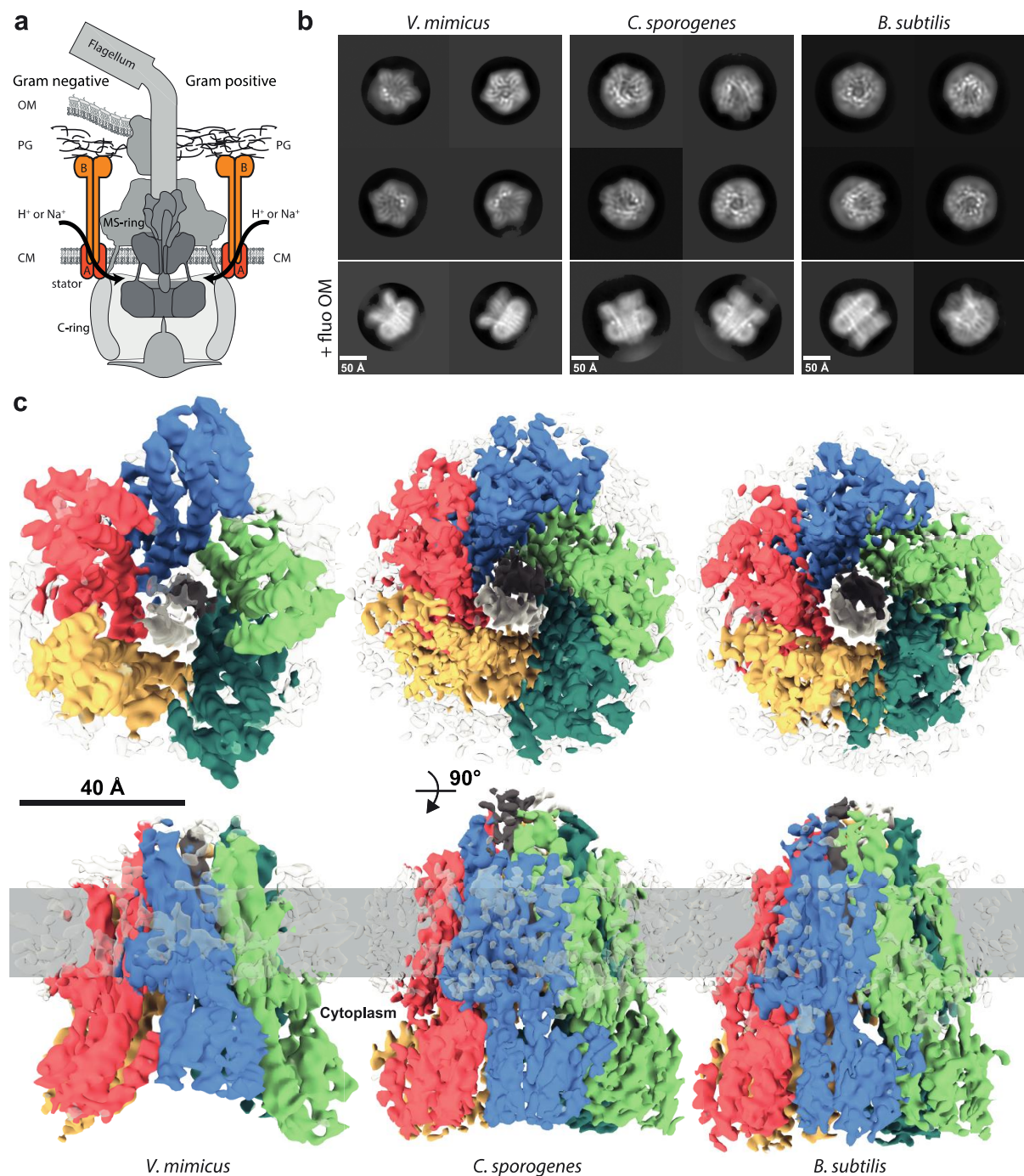


**Fig. 1: Stator complexes from multiple organisms have a MotA<sub>5</sub>MotB<sub>2</sub> stoichiometry.** **a**, Composite cartoon showing the general organisation of bacterial flagellar complexes in Gram-negative (left side) and Gram-positive (right side) bacteria with major components labelled. Stator complexes are orange and rotor components, MS- and C-ring, are grey. OM, outer membrane; CM, cytoplasmic membrane; PG, peptidoglycan. **b**, 2D class averages of cryo-EM particles of stator complexes from the bacterial species indicated. Upper panels are representative 'top' views of the 5:2 complexes. Lower panels are 'side' views from data collected in the presence of fluorinated octyl maltoside. **c**, Cryo-EM volumes of stator

complexes from the three bacterial species. The MotA subunits are coloured pink, blue, green, teal, and yellow, and the centrally located MotB subunits white and dark grey. Bound detergent is shown as transparent density at the periphery. Upper panels show views from the cytoplasm, lower panels show side views with the likely membrane location (assigned from the position of the detergent micelle and from simulations; Extended Data Fig. 7) indicated by the grey bar.

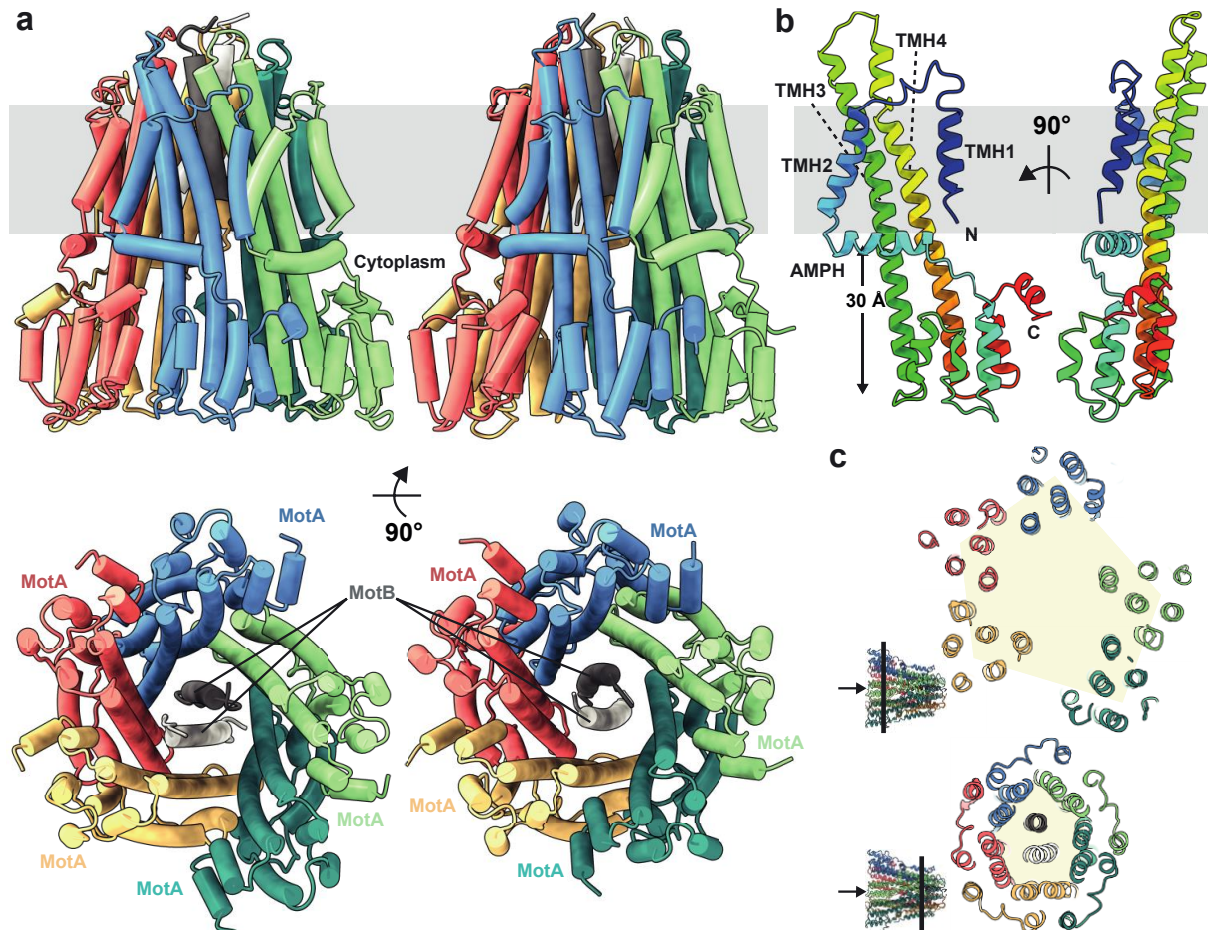


**Fig. 2: Structures of stator complexes from *C. sporogenes* and *B. subtilis*.** **a**, The *C. sporogenes* (left) and *B. subtilis* (right) stator complexes are shown as cartoon representations and coloured as in Figure 1C. Upper panel, side view with membrane indicated in grey. Lower panel, view from the cytoplasm. **b**, Two views of a single MotA subunit (*C. sporogenes*) coloured from blue at the N terminus to red at the C terminus. **c**, Slabs (viewed from cytoplasm) through the *C. sporogenes* complex at the indicated positions on the inset structure (arrow indicates the cytoplasmic side of the complex). Distortion of the MotA subunits from a regular pentagon arrangement becomes more extreme in the cytoplasmic regions.



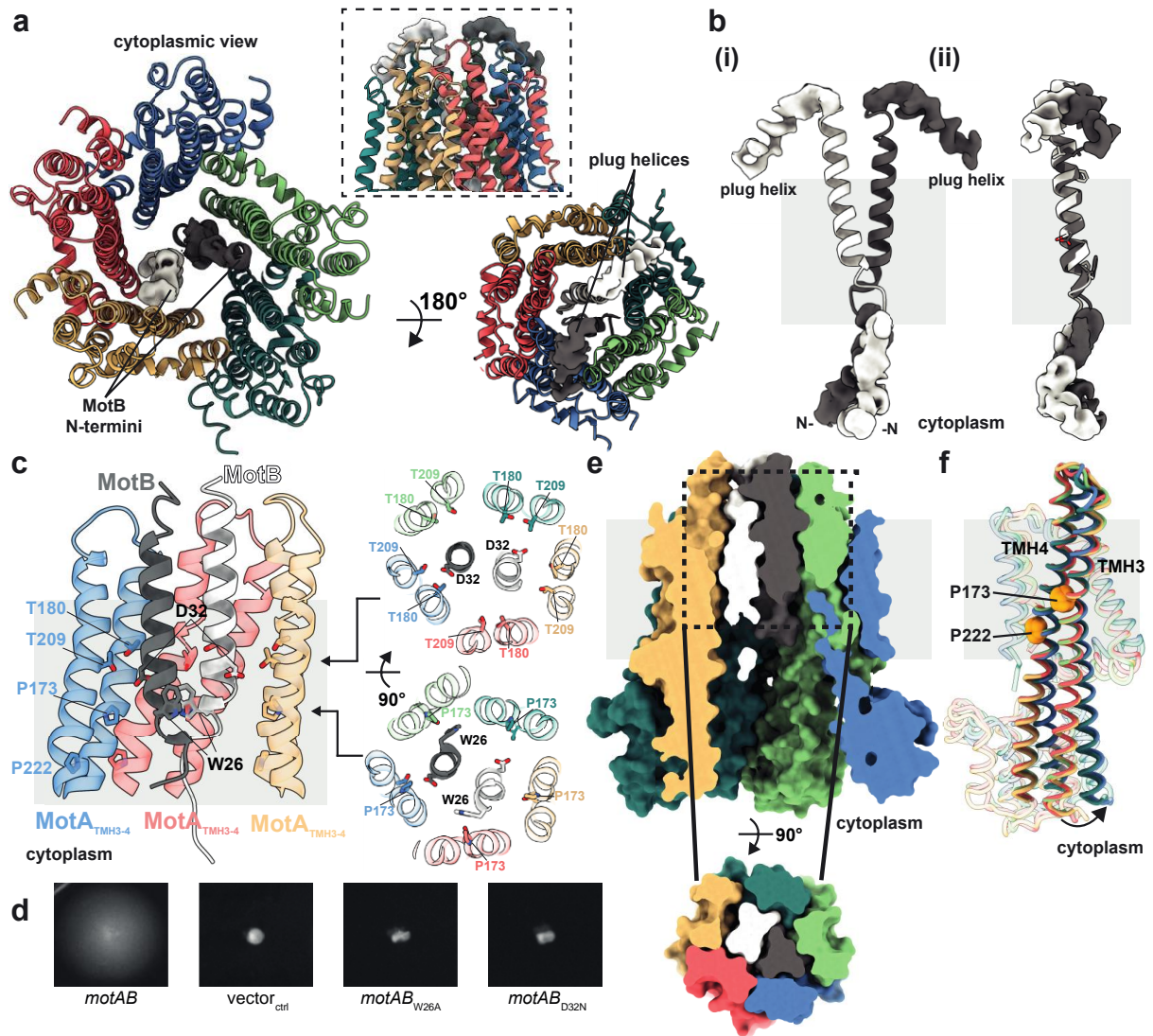


**Fig. 3: Functionally critical regions of the stator complex.** **a**, Structure of the *C. sporogenes* stator complex shown as cartoon representations coloured as in Figures 1 and 2 with the unmodeled density for the MotB N-terminal extensions (Left) and plug helices (Right) shown. Inset shows plug densities in context of top of complex. **b**, (i) Isolated MotB dimer extracted from the *C. sporogenes* stator complex and (ii) superposition of the TMHs of the two MotB chains showing the relative rotation of the N-terminal extensions and plug helices. The location of the membrane is indicated in grey. **c**, The environment around MotB<sub>D32</sub> within the membrane. (Left) Only the core MotA helices within the transmembrane region are shown and the two copies of MotA at the front of the view are removed. (Right) Slabs through the stator complex core at the indicated heights. Residue numbering is that of the *E. coli* MotAB stator complex but displayed on the *C. sporogenes* stator complex structure. Residues from MotA are coloured to denote the subunit, MotB are labelled in black. **d**, Motility in soft agar of *E. coli* RP6894 ( $\Delta$ motAB) complemented with plasmids expressing *motAB* with the indicated mutations or the vector control (vector<sub>ctrl</sub>). **e**, Surface representation of the model shows close packing. (Top) Side view with front of complex removed. (Bottom) Top-down view of the slab indicated by dashed lines. **f**, Overlay of the five copies of the *C. sporogenes* MotA chain reveals they fall into two conformational classes which differ in the degree of flexing at the highlighted prolines.

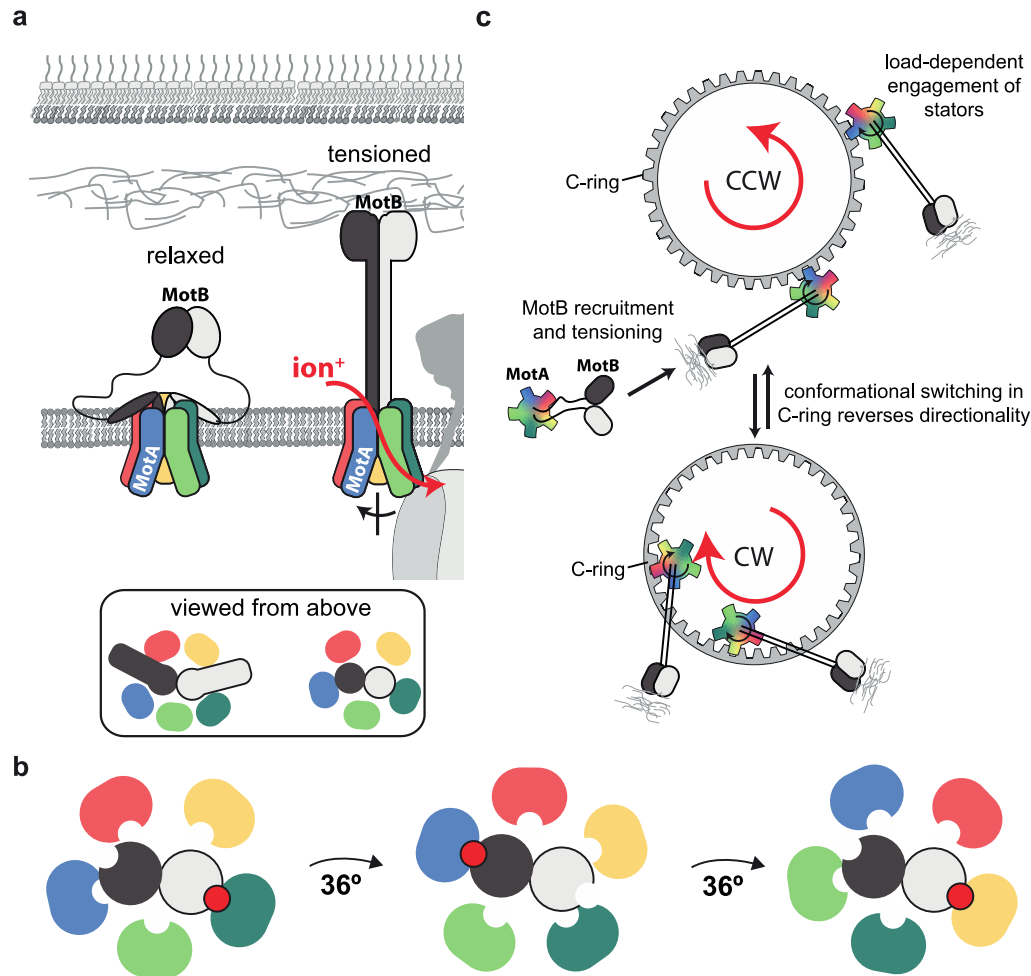


**Fig. 4: Mechanistic model for the generation of bi-directional flagellar torque.** **a**, Activation of the stator complex from the structurally resolved state (here termed 'relaxed') to form a 'tensioned' state permissive to ion-flow. This conformational change is likely driven by interactions between the C-terminal peptidoglycan binding domains (black and white ovals) of MotB and the peptidoglycan layer, as well as interactions between the stator complex and the C-ring complex. **b**, Cartoon showing top views of the intra-membrane core of the stator complex, viewed from above (extracytoplasmic side), with five MotA chains surrounding two MotB subunits. Bound ions are shown as red spheres. Ion flow leads to rotation of the MotA ring through alternating formation of MotB-ion-MotA interactions by the two MotB chains that processes around the surrounding MotA subunits. **c**, View from above of a model describing how a stator complex that rotates in one direction can drive either clockwise (CW) or counterclockwise (CCW) rotation of the flagellum depending on the conformational state of the C-ring.



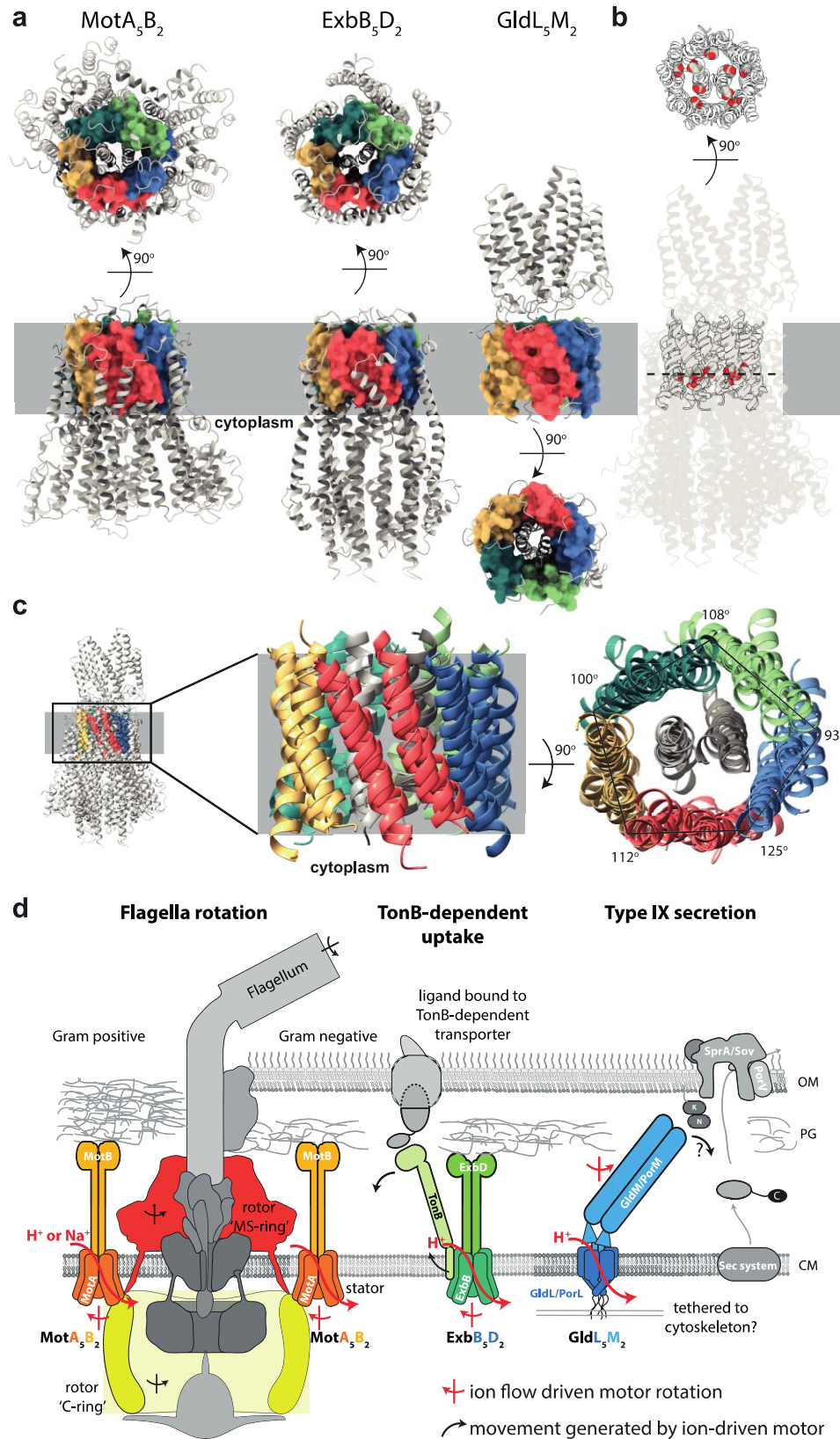


**Fig. 5: Conservation of core architecture between diverse families of ion-driven motors. a,** Representatives of three ion-driven motor families that share a common structural core. Complexes are shown as grey cartoons with helices equivalent to those in the MotA inner ring displayed in coloured surface representation. **b,** Overlay of the three complexes (common core in grey cartoons, other structure semi-transparent cartoons). Mechanistically essential charged residues within the common core (space filling side chains; C, grey; O, red) occur at the same height with respect to the membrane irrespective of whether they occur on the MotA- or MotB-equivalent chain. **c,** Overlay of the common core of the three complexes. The distortion from pentamer symmetry within the membrane is shared between all three families **d,** Cartoon summarising the updated view of how the three families of ion-driven motors are coupled to their different biological effects. Note that ion movement is proposed to drive rotation of the central subunits in GldLM but of the peripheral subunits in MotAB/ExbBD. The identity of the tether for GldL is unknown but is hypothesised to be a cytoskeletal component <sup>42</sup>. OM, outer membrane; CM, cytoplasmic membrane; PG, peptidoglycan

**Table 1:** Cryo-EM data collection, refinement and validation statistics

	<i>C. sporogenes</i> MotAB (EMDB-10895) (PDB ID 6YSF)	<i>B. subtilis</i> MotAB (EMDB-10899) (PDB ID 6YSL)	<i>V. mimicus</i> PomAB (EMDB-10901)	<i>E. coli</i> ExbBD (EMDB-10902)	<i>P. savastanoi</i> ExbBD (EMDB-10897)
<b>Data collection and processing</b>					
Magnification	165,000	165,000	165,000	165,000	165,000
Voltage (kV)	300	300	300	300	300
Electron exposure (e-/Å <sup>2</sup> )	48	48	48	48	48
Defocus range (µm)	1.0-3.0	1.0-3.0	1.0-3.0	1.0-2.5	1.0-3.0
Pixel size (Å)	0.822	0.822	0.822	0.822	0.822
Symmetry imposed	C1	C1	C1	C1	C1
Initial particle images (no.)	1,998,900	1,532,430	2,383,022	2,045,350	1,342,937
Final particle images (no.)	314,230	122,615	244,654	227,700	65,617
Map resolution (Å)	3.4	3.5	4.2	4.6	3.8
FSC threshold	0.143	0.143	0.143	0.143	0.143
Map resolution range (Å)	3.2-5.2	3.3-6.0	3.9-6.5	4.0-6.5	3.6-6.1
<b>Refinement</b>					
Initial model used (PDB code)	None	None			
Model resolution (Å)	3.4	3.5			
FSC threshold	0.143	0.143			
Model resolution range (Å)	3.2-5.2	3.3-6.0			
Map sharpening B factor (Å <sup>2</sup> )	-117	-104			
Model composition					
Non-hydrogen atoms	10220	10128			
Protein residues	1327	1324			
Ligands	0	0			
B factors (Å <sup>2</sup> )					
Protein	53	99			
Ligand	NA	NA			
R.m.s. deviations					
Bond lengths (Å)	0.004	0.007			

Bond angles (°)	0.757	1.425
Validation		
MolProbity score	2.15	1.85
Clashscore	13.66	5.93
Poor rotamers (%)	0.90	0.47
Ramachandran plot		
Favored (%)	91.47	90.92
Allowed (%)	8.53	9.01
Disallowed (%)	0.00	0.08
Model-vs-map FSC at FSC=0.5	3.5	3.8
EMRinger score	2.12	1.19